On the Propagation of Concentration Polarization from Microchannel−Nanochannel Interfaces Part II: Numerical and Experimental Study

Thomas A. Zangle, Ali Mani, and Juan G. Santiago*

Department of Mechanical Engineering, Stanford University, 440 Escondido Mall, Building 530, Room 225, Stanford, California 94305

We present results of a combined computational and experimental study of the propagation of concentration polarization (CP) zones in a microchannel−nanochannel system. Our computational model considers the combined effects of bulk flow, electromigration, and diffusion and accurately captures the dynamics of CP. Using wall charge inside the nanochannel as a single fitting parameter, we predict experimentally observed enrichment and depletion shock velocities. Our model can also be used to compute the existence of CP with propagating enrichment and depletion shocks on the basis of measured ion mobility and wall properties. We present experiments where the background electrolyte consists of only a fluorescent ion and its counterion. These results are used to validate the computational model and to confirm predicted trends from an analytical model presented in the first of this two-paper series. We show experimentally that the enrichment region concentration is effectively independent of the applied current, while the enrichment and depletion shock velocities increase in proportion to current density.

Introduction

In electrokinetic nanochannels, the number of diffuse ions associated with electric double layers (EDLs) is of the same order as the number of background ions leading to an imbalance of current transport by counter- and coions.[1−4] As we presented in Part I,[5] this ionic flux imbalance drives concentration polarization (CP). In Part I, we found that, under conditions with high-Dukhin number and coion mobility, CP coupled with bulk flow can create propagating enrichment and depletion shocks. These shocks can have a long-range influence on a system which contains both nano- and microchannels. Systems combining nanochannels and channels with micrometer or larger characteristic length scales are being used for a variety of applications including increasing sample ion concentration,[6] analyzing DNA,[7] and detecting single molecules (and single ligand-binding pairs) with nanopores.[8]

There have been a significant number of experimental studies of microchannel−nanochannel interfaces. Wang et al.[9] reported the use of CP to generate high-focusing ratios of an ionic protein near a microchannel−nanochannel junction. CP has since been used for preconcentration with nanofluidic channels[6] and ion-permselective membranes.[10,11] Kim et al.[2] experimentally

observed vortices at the interface between a microchannel and a nanochannel.

Studies of colloids and nanoporous membranes were among the earliest basic experimental investigations of CP. Rubinshtein et al.[12] reported the use of a gel to stabilize the liquid on the depletion side of a nanoporous membrane suppressing the instability mechanism which causes overlimiting conductance. In a microchannel system, Pu et al.[1] performed imaging with Fluorescein and reported enrichment and depletion zones below a threshold concentration of 3 mM sodium borate with a 60 nm nanochannel. Dhopeshwarkar et al.[4] reported focused peaks of Fluorescein moving away from the cathode side interface between a microchannel and a nanoporous hydrogel plug. Finally, Hlushkou et al.[13] performed experiments showing the effects of neutral or negatively charge hydrogel plugs on the enrichment of size-excluded analytes.

The typical electrolyte system used in previous experiments consists of a buffer ion, its coion, and a third, observable, fluorescent ionic species initially present in low concentration relative to the two other "background" ions. To date, outside of our own work,[3] we are aware of no microchannel CP experiments which directly observed the concentration distribution of one of two dominant ions which make up an electrolyte.[1,2,4,9,10]

Additionally, previous experiments were typically performed at potentiostatic (constant voltage) conditions.[1,2,4,13] This makes comparisons to models difficult as current density (and not voltage) directly dictates local ion transport throughout the system. When CP shocks propagate, the microchannel−nanochannel system resistance is dominated by the large resistance of the depletion region. However, as has been observed in studies of nanoporous membranes,[14] conditions in the depletion region may

* To whom correspondence should be addressed. E-mail: juan.santiago@stanford.edu; fax: (650) 723-7657.

(1) Pu, Q.; Yun, J.; Temkin, H.; Liu, S. *Nano Lett.* **2004,** *4,* 1099–1103.
(2) Kim, S. J.; Wang, Y.-C.; Lee, J. H.; Jang, H.; Han, J. *Phys. Rev. Lett.* **2007,** *99,* 044501.
(3) Zangle, T. A.; Mani, A.; Santiago, J. G. Proceedings of *μ* TAS 2007, Paris, France, October 7–11, 2007; Viovy, J. L., Tabeling, P., Descroix, S., Malaquin, L., Eds.; Chemical and Biological Microsystems Society: San Diego, CA, 2007; Vol. 2, pp 1204–1206.
(4) Dhopeshwarkar, R.; Crooks, R. M.; Hlushkou, D.; Tallarek, U. *Anal. Chem.* **2008,** *80,* 1039–1048.
(5) Mani, A.; Zangle, T. A.; Santiago, J. G. *Langmuir* **2009,** *25,* 3898-3908.
(6) Wang, Y.-C.; Han, J. *Lab Chip* **2008,** *8,* 392–394.
(7) Pennathur, S.; Baldessari, F.; Santiago, J. G.; Kattah, M. G.; Steinmen, J. B.; Utz, P. J. *Anal. Chem.* **2007,** *79,* 8316–8322.
(8) Sexton, L. T.; Horne, L. P.; Sherrill, S. A.; Bishop, G. W.; Baker, L. A.; Martin, C. R. *J. Am. Chem. Soc.* **2007,** *129,* 13144–13152.
(9) Wang, Y.-C.; Stevens, A. L.; Han, J. *Anal. Chem.* **2005,** *77,* 4293–4299.
(10) Kim, S. M.; Burns, M. A.; Hasselbrink, E. F. *Anal. Chem.* **2006,** *78,* 4779–4785.
(11) Kim, S. J.; Han, J. *Anal. Chem.* **2008,** *80,* 3507–3511.
(12) Rubinshtein, I.; Zaltzman, B.; Pretz, J.; Linder, C.; Russ, J. *Electrochemistry* **2002,** *38,* 853–863.
(13) Hlushkou, D.; Dhopeshwarkar, R.; Crooks, R. M.; Tallarek, U. *Lab Chip* **2008,** *8,* 1152–1162.
(14) Block, M.; Kitchener, J. A. *J. Electrochem. Soc.* **1966,** *113,* 947–953.

be governed by reaction equilibria (e.g., dissociation of water[15]) which have not been considered in microchannel CP models to date. Furthermore, constant current conditions yield linear growth of the enrichment and depletion regions with time (cf. Figure 4), which simplifies comparison to models. However, constant current and constant voltage demonstrate essentially the same effects with a difference only in the rate at which CP propagates.

In Part I,[5] we presented and discussed two models which describe CP, including CP with propagation. Our area-averaged model was presented in terms of the Boltzmann equilibrium concentration, c_0. c_0 equals the centerline counterion concentration for a channel with negative surface charge and nonoverlapped EDLs. In the case of overlapped EDLs, c_0 is a concentration associated with evaluating the Boltzmann distribution at zero potential relative to the potential in a hypothetical reservoir. As discussed in Part I, the centerline concentration is equal to $c_0 \exp(-z_i e\psi|_{y=0}/kT)$, where $\psi|_{y=0}$ is the centerline potential obtained by solving the Poisson−Boltzmann equation with boundary conditions imposed at the walls ($y = \pm h/2$). c_0 varies in x and is fixed at the inlet and outlet of the system to the value of ionic concentration at end-channel reservoirs where $\psi = 0$. We found that the coupling of CP and bulk flow is captured analytically by a system of PDEs for the evolution of c_0 as follows:

$$\frac{\partial}{\partial t}(hfc_0) + \frac{\partial}{\partial x}[h(\bar{u}^p f_2^p + u_0^e f_2^e + \nu_2 z_2 FEf)c_0] = \frac{\partial}{\partial x}\left[hD_2 f \frac{\partial c_0}{\partial x}\right] \tag{1}$$

$$\frac{\partial}{\partial t}\left(hfc_0 - \frac{2\sigma}{z_1 F}\right) + \frac{\partial}{\partial x}[h(\bar{u}^p f_1^p + u_0^e f_1^e + \nu_1 z_1 FEf)c_0 - 2\nu_1 E\sigma]$$
$$= \frac{\partial}{\partial x}\left[hD_1 f \frac{\partial c_0}{\partial x} - \frac{2D_1}{z_1 F}\frac{\partial \sigma}{\partial x}\right] \tag{2}$$

where $u_0^e = (-\varepsilon\zeta E/\eta)$ is the Helmholtz−Smoluchowski velocity, and $\bar{u}^p$, the area-averaged pressure-driven flow velocity, is determined from the conservation of mass

$$\frac{\partial}{\partial x}(h\bar{u}^p + hu_0^e f^e) = 0 \tag{3}$$

The functions f, f^e, f_1^p, f_2^p, f_1^e, and f_2^e are defined in Part I. These functions describe the effect of finite EDLs; h is the local channel height; ν_1 and ν_2 are the mobilities of the positive and negative species; z_1 and z_2 are the valences of the positive and negative species. We use the anion diffusivity, D_2, to approximate diffusion effects; ζ is zeta potential; σ is wall charge; ε is permittivity; F is Faraday's constant; η is viscosity. Equations 1−3 can be discretized and solved numerically for c_0, E, and $\bar{u}^p$ to generate predictions of CP and CP propagation for more general cases than we considered with the simple model in Part I.

The second model presented in Part I (the simple model) showed that a nonzero slope of the channel height, $\partial h/\partial x \neq 0$, gives rise to CP regardless of channel height. This is consistent with Dukhin and Shilov's work on polarization around a spherical particle.[16] Dukhin and Shilov showed that net neutral concentration is transferred into or out of the bulk solution whenever current crosses into or out of an EDL. Within the EDL, more current is carried by counterions to the wall charge than coions. Local enrichment occurs because of an ionic flux imbalance when more counterions emerge from an EDL than are required to carry current in the bulk solution. In our system, enrichment occurs at the micro/nanochannel interface on the cathode side

(15) Probstein, R. F. *Physicochemical Hydrodynamics: An Introduction*, 2nd ed.; John Wiley & Sons, Inc.: New York, 2003.
(16) Dukhin, S. S.; Shilov, V. N. *Kolloidn. Zh.* **1969**, *31*, 706–713.
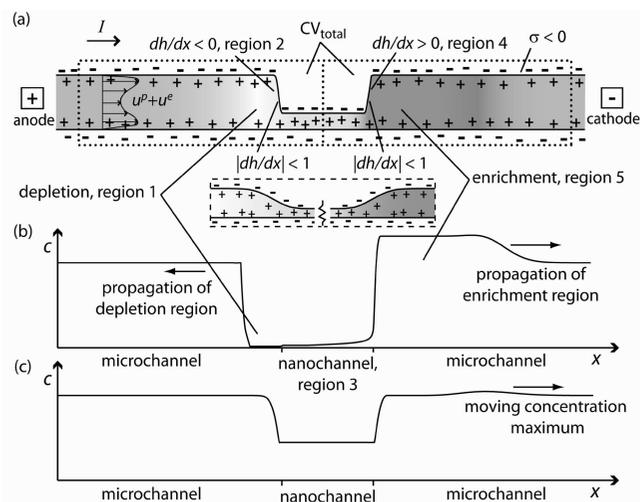
Figure 1. Schematic of microchannel−nanochannel−microchannel system. (a) The sign of the wall charge and the shallow micro-to-nano- and nano-to-micro interfaces shown. Dotted lines depict control volumes (CV) used to derive the enrichment region concentration increase. Simulation results (concentration profiles) show cases where propagating CP occurs (b) and when there are negligible CP and no propagation of CP zones (c). In b, the regions of strong depletion (anode side) and significant enrichment (cathode side) propagate up and downstream, respectively. In c, the final concentration in the microchannels is approximately equal to the initial value.

where $\partial h/\partial x > 0$ (Figure 1a, region 4). Similarly, at the anode side interface (region 2) $\partial h/\partial x < 0$, counterions enter the EDLs, and there is a local depletion of c_0. In Part I, we found that while a polarization of net charge (CP) always occurs to some extent in a microchannel−nanochannel−microchannel system, propagation of accumulation and depletion regions is governed by two key nondimensional parameters. One is an inverse Dukhin number, $c_r^* h_n^* = (\nu_1 z_1 - \nu_2 z_2)Fh_n c_r/(-2\nu_1\sigma)$, which describes the ratio of bulk conductivity to EDL conductivity, and the other is the mobility of the coion divided by the electroosmotic mobility, $\nu_{2n}^* = \nu_2 z_2 F\eta/\zeta_n\varepsilon$. Low $c_r^* h_n^*$ values and high ν_{2n}^* values result in sufficiently strong depletion at the anode side interface to cause negative characteristic velocities in the depletion region. Under these conditions, a CP depletion shock propagates into the anode side microchannel (region 1); simultaneously, an enrichment shock propagates into the cathode side channel (region 5). High values of $c_r^* h_n^*$ and low values of ν_{2n}^* result in positive characteristic velocities in the depletion zone, and no shock propagation is observed. Therefore, the sign of the characteristic velocity in the depletion region fully determines the existence of CP with propagation.

In this paper, we present computations on the basis of eqs 1−3 for a range of conditions which we also examined experimentally. The experiments and predictions presented here are in the high PeL/h regime where propagation of CP zones is readily detectable and where CP zone interface widths are small relative to the channel length. These results show that, because of CP with propagation, a nanochannel can have significant long-range (e.g., ∼cm long) effects in a typical hybrid microchannel−nanochannel system. We show that computations based on eqs 1−3 using independent measurements of system parameters with no fitting parameters can be used to predict whether or not CP shocks will propagate. For the first time, we present experiments where the background electrolyte consists of only a fluorescent ion and its counterion. We use well-controlled experiments at constant current conditions and quantify the spatiotemporal development of CP with propagation. These experiments confirm that the simple model of Part I provides useful scaling and intuition
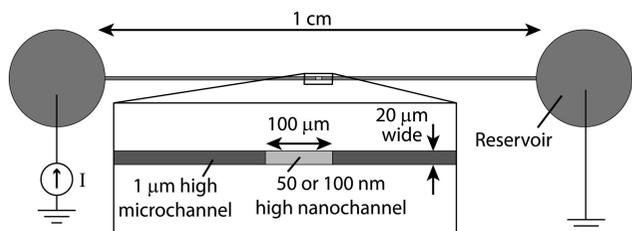
Figure 2. Schematic of experimental setup of microchannel−nano-channel−microchannel system. The device was fabricated using a two dry etch process on fused silica. We filled channels with a solution where lithium ions and fluorescent Alexa Fluor ions (in a small number of cases only sodium and Fluorescein ions) formed the primary electrolyte. We applied constant current using a high-voltage (source-and-measure) power supply.

regarding propagating enrichment and depletion regions. In computations using nanochannel wall charge as the only fitting parameter, we show excellent agreement between predictions and experimentally measured enrichment and depletion shock velocities.

Numerical Study

This paper considers devices fabricated with the simple microchannel−nanochannel−microchannel geometry depicted in Figures 1a and 2. The numerical model solves species flux equations which are area-averaged (integrated over the channel height and assumed uniform across the channel width) resulting in one-dimensional (along axial length), unsteady equations for species, electric flux, and ionic current. As discussed above, this area-averaged model includes the effects of EDLs in both the nano- and microchannels using the f factors given in Part I.

Here, we will give the solution algorithm for eqs 1−3. As shown in Part I, we can rewrite eq 3 as

$$\bar{u}^p = (Q - hf^e u_0^e)/h \qquad (4)$$

where $Q = \int_{x_1}^{x_2} f^e u_0^e h^{-2})\mathrm{d}x / \int_{x_1}^{x_2} h^{-3}\mathrm{d}x$ is the volume flow rate per unit width. Substituting this expression for Q into eq 4 results in an explicit expression for $\bar{u}^p$ in term of u_0^e. Using this expression for $\bar{u}^p$, we subtract eq 1 from eq 2 to obtain an expression for conservation of current:

$$\frac{\partial}{\partial t}\left(-\frac{2\sigma}{z_1 F}\right) + \frac{\partial}{\partial x}[h(\bar{u}^p(f_1^p - f_2^p) + u_0^e(f_1^e - f_2^e) +$$
$$(\nu_1 z_1 - \nu_2 z_2)FEf)c_0 - 2\nu_1 E\sigma] =$$
$$\frac{\partial}{\partial x}\left[h(D_1 - D_2)f\frac{\partial c_0}{\partial x} - \frac{2D_1}{z_1 F}\frac{\partial \sigma}{\partial x}\right] \quad (5)$$

The model allows us to study the effect of spatial and temporal variations of σ in eq 5 (e.g., with local ion densities). However, we here study mostly the case of fixed σ for simplicity. Also for simplicity, we neglect the diffusion term in eq 5 but keep the diffusion term in eq 1 to approximately capture the effects of diffusion on concentration profiles.[5] Next, using the solution for $\bar{u}^p$ and u_0^e, we integrate eq 5 along the axial direction to obtain an integral equation for E:

$$\left\{\left[(\nu_1 z_1 - \nu_2 z_2)Ff - \frac{\varepsilon\zeta}{\eta}(f_1^e - f_2^e - f_1^p f^e + f_2^p f^e)\right]hc_0 - 2\nu_1\sigma\right\}E -$$
$$\frac{\varepsilon(f_1^p - f_2^p)c_0}{\eta\int_{x_1}^{x_2}\frac{\mathrm{d}x}{h^3}}\int_{x_1}^{x_2}\frac{f^e\zeta E}{h^2}\mathrm{d}x = \frac{I}{Fz_1} \quad (6)$$

where I is fixed for the constant current conditions considered here. To time advance the one-dimensional partial differential
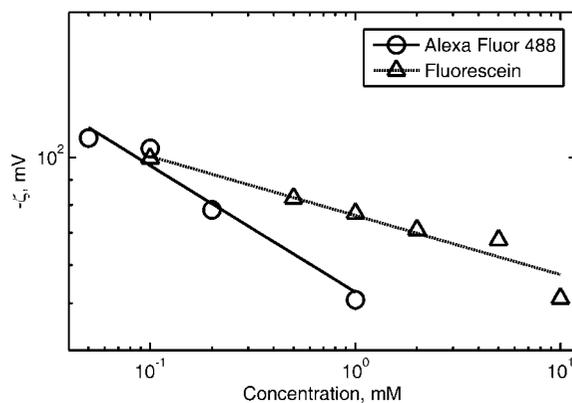
Figure 3. Zeta potential measurement results versus Alexa Fluor 488 and sodium fluorescein concentration. A power law fit of the form $\zeta = -aC^b$ gave $a = 0.0527$ V/mM^b and $b = -0.261$ for Alexa Fluor 488 and $a = 0.0760$ V/mM^b and $b = -0.122$ for Fluorescein. Data are shown over the concentration range used in CP experiments.

eq 1, one can first obtain the previously discussed f-factors and ζ, which are known functions of c_0, and solve eq 6 to obtain $E(x)$. Then, substituting $E(x)$ yields u_0^e, which can be used to obtain $\bar{u}^p$, providing all of the terms in eq 1.

For our computations, we used a one-dimensional grid for spatial discretization of eqs 1 and 6 with a grid spacing of 2 μm for the nanochannel and 20−100 μm for the microchannels. The height jumps at the channel interfaces were modeled as smooth gradients across a length of about 5 μm. The integral in eq 6 was discretized using a second-order rectangle rule.[17] We used a Roe scheme[18] to discretize the nonlinear flux and employed a second-order central difference[17] to approximate the diffusive flux in eq 1. For time integration, we used a first-order implicit time advancement method[17] to enhance robustness of the numerical solution. We conducted a mesh and time step refinement study to ensure that the solutions are unbiased by discretization errors.

We computed the dynamics of CP as a function of the two major parameters discussed in Part I: $c_r^* h_n^*$ and ν_{2n}^* (cf. Figure 5). To this end, we performed 732 full simulations of the microchannel−nanochannel system for conditions covering the range of $c_r^* h_n^*$ and ν_{2n}^* considered experimentally. We chose all other parameters to match the experimental conditions: $h_n = 50$ nm, $h_m = 1$ μm, $I = 1 \times 10^{-4}$ A/m, $t_{final} = 100$s, $z_1 = 1$, $z_2 = -2$, $L_{nano} = 100$ μm, $L_{total} = 10$ mm, $c_r = 2$ mM, and $\nu_2/\nu_1 = 0.35$ (unless otherwise noted). The parameters $c_r^* h_n^*$ and ν_{2n}^* determined the wall charge, σ, and the mobility of the anionic species, ν_2, for each condition. For these computations, the wall charge was assumed to be constant and uniform throughout the channel system. We note that dynamics of wall charge is a complex and open problem in this field[19,20] and that the assumptions we use here suffice to capture the major trends observed in experiments. In separate computations, for direct quantitative comparison to experiments (cf. Figure 4), we used the nanochannel wall charge, σ_{nano}, as a single fitting parameter. We adjusted σ_{nano} until the depletion region shock velocity matched the experimental depletion shock velocity.[21]

Experimental Section

Materials and Instrumentation. We filtered deionized (DI) water prior to use with 0.2 μm pore syringe filters (Nalge Nunc

(17) Moin, P. *Fundamentals of Engineering Numerical Analysis*, 1st ed.; Cambridge University Press: Cambridge, U.K., 2001.
(18) Leveque, R. J. *Finite Volume Methods for Hyperbolic Problems*, 1st ed.; Cambridge University Press: Cambridge, U.K., 2002.
(19) Stein, D.; Kruithof, M.; Dekker, C. *Phys. Rev. Lett.* **2004**, *93*, 035901.
(20) van der Heyden, F. H. J.; Stein, D.; Dekker, C. *Phys. Rev. Lett.* **2005**, *95*, 116104.
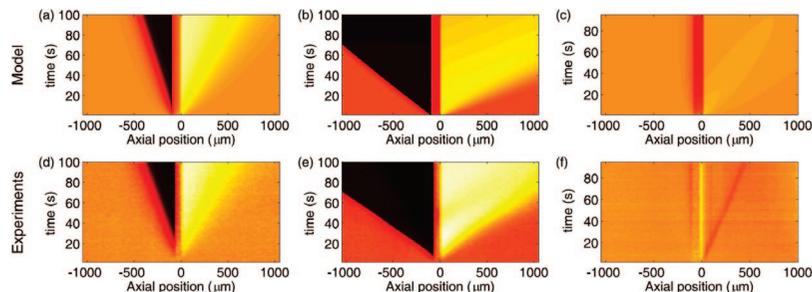
Figure 4. Representative simulations and experimental visualizations of ion transport and accumulation in our micro-nano–microchannel system with 1 μm high microchannels. We show predicted spatiotemporal diagrams (ion concentration vs time and axial position) for (a) $I = 200$ pA and (b) $I = 800$ pA. Both a and b are for 1 mM Alexa Fluor 488, 50 nm high nanochannel, and $\sigma_{nano} = 0.25\,\sigma_{micro}$. Also shown are results for (c) $I = 800$ pA, 10 mM Fluorescein, 100 nm high nanochannel, and $\sigma_{nano} = \sigma_{micro}$ (no fitting parameter in this thin-EDL case). In the second row, we show experimental results for (d) $I = 200$ pA and (e) $I = 800$ pA. Both d and e used 1 mM Alexa Fluor 488 and 50 nm high nanochannel. Also shown are results for (f) $I = 800$ pA, 10 mM Fluorescein, and 100 nm high nanochannel. For the conditions of experiments d and e, the model captures the essential observed features of propagating depletion (left side) and enrichment (right side) zones and the proportionality of shock velocities with applied current. The model (in c) successfully predicts a slight disturbance and steady-state microchannel concentrations approximately equal to the initial values as observed in experiment f.
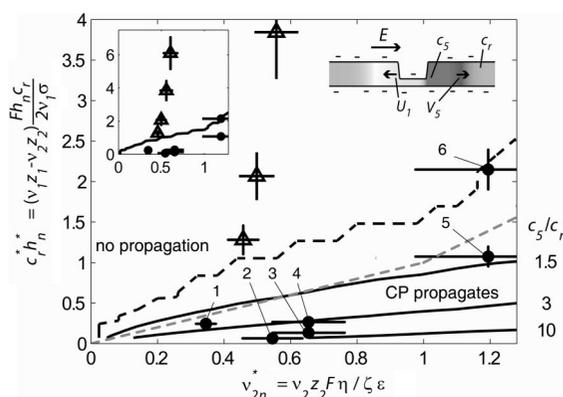
Figure 5. Phase diagram showing CP magnitude, c_5/c_r, from computations versus $c_r^* h_n^*$ and v_{2n}^* and experimental observations covering the major parametric regimes. Contours reflect magnitude of computed c_5/c_r from 732 simulated conditions. The black dashed line is an approximate contour of $U_1/V_5 = 0$, a practical cutoff defining the boundary between conditions with and without propagating shocks. U_1/V_5 is the ratio of the characteristic velocity in the depletion region to the enrichment shock velocity. The gray dashed line is the phase boundary between conditions with and without propagation predicted from the simple model of Part I. Filled circles and open triangles denote observations with and without CP propagation, respectively. The numbers next to the filled circles indicate the concentration enrichment measurements shown in Table 1. Vertical and horizontal error bars represent the propagation of uncertainties in measured ζ (on the basis of reservoir concentration) and ion mobility on $c_r^* h_n^*$ and v_{2n}^* with 95% confidence intervals. (Only one observation of $c_5/c_r = 4.7$ was made for the Fluorescein case at $c_r^* h_n^* = 0.25$, $v_{2n}^* = 0.35$.) Top left insert shows an enlarged view of the $c_r^* h_n^*$ and v_{2n}^* domain containing one additional experiment. Schematic at the top right shows measurement locations of concentrations and velocities.

International, Rochester, NY). We chose Alexa Fluor 488 (carboxylic acid succinimidyl ester, Molecular Probes, Eugene, OR) dye for insensitivity to pH and low rate of photobleaching.[22] Upon dissolution in deionized water, the electrolyte consists of the divalent Alexa Fluor anion and the lithium cation. In limited cases, we also used sodium Fluorescein (J.T. Baker, Phillipsburg, NJ) at higher ionic strength (because of its strong solubility in water) to qualitatively determine if CP shocks propagate. Fluorescein fluorescence has a strong dependence on pH and is strongly susceptible to photobleaching (relative to Alexa Fluor) precluding us from using Fluorescein as a quantitative measure of ion concentration. These electrolyte systems are unbuffered, and therefore, pH is determined by equilibrium with dissolved carbon dioxide and electrolysis at the electrodes. We measured pH $\approx$ 5 before the start of experiments which we attributed to

Table 1. Summary of Experimental Conditions and Measured Values Presented in Figure 5

condition number	electrolyte	c_r (mM)	h_n (nm)	measured concentration enrichment[a]	number of realizations
1	Fluorescein	0.1	100	4.7	1
2	Alexa Fluor	0.05	50	7.36 ± 0.41	18
3	Alexa Fluor	0.1	50	4.81 ± 0.45	19
4	Alexa Fluor	0.1	100	2 ± 0.16	18
5	Alexa Fluor	1	50	1.35 ± 0.11	18
6	Alexa Fluor	1	100	1.5 ± 0.18	2

[a] Stated range is uncertainty on the mean value with 95% confidence.

the influence of carbon dioxide. To estimate the effect of pH during the experiment, we assume well-mixed reservoirs, a maximum applied current of 4 nA, an experiment duration of 100 s, and a typical well volume of 40 μL. This gives a maximum total concentration of 1×10^{-7} M hydronium ions produced at the anode. This is negligible relative to the initial concentration of hydronium ($\sim 10^{-5}$ M) from atmospheric carbon dioxide resulting in negligible change in pH.

We captured images using an upright, epifluorescent microscope (Olympus IX-70, Happauge, NY) with a dichroic filter cube with cutoffs at 493, 505 (dichroic), and 500 nm (Z488BP, Chroma Technology Corp., Rockingham, VT) and 10×, numerical aperture (NA) 0.4 (UPlanApo) or 20×, 0.5 NA (UPlanFl) objectives (Olympus, Happauge, NY). We recorded images using a 12-bit, intensified charge-coupled device (CCD) camera (IPentaMAX, Roper Scientific, Trenton, NJ) using a $0.31\times$ demagnifier (Diagnostic Instruments, Inc. Sterling Heights, MI) to increase field of view while preserving resolution. A manually adjustable pulse generator (BNC 555, Berkeley Nucleonics Corporation, San Rafael, CA) set the frame rate. We used a high-voltage source-and-measure power supply (Sourcemeter 2410, Keithley Instruments, Inc., Cleveland, OH) to control current density. The experimental setup is shown schematically in Figure 2.

(21) We also explored a version of the model where the surface charge was varied locally and in real time during the computation. This used an empirical fit for zeta potential as a function of local ion density (cf. Figure 3) and the full Poisson–Boltzmann equation to relate surface charge to zeta potential. We found this model performed worse than the fixed surface charge model (e.g., in predicting V_1, V_5, and c_5). We hypothesize that this is partly because our CP and transport processes are fast (typically 100 s or less) relative to the time scale for equilibrium between the wall charge and bulk solution. See, for example, Kirby, B. J.; Hasselbrink, E. F. *Electrophoresis* **2004**, *2025*, 2187–2202.

(22) Panchuk-Voloshina, N.; Haugland, R. P.; Bishop-Stewart, J.; Bhalgat, M. K.; Millard, P. J.; Mao, F.; Leung, W.-Y.; Haugland, R. P. *J. Histochem. Cytochem.* **1999**, *47*, 1179–1188.

Preliminary Quantifications of Electrophoretic and Electroosmotic Mobilities. The mobility of the Alexa Fluor 488 dianion was determined experimentally given the known mobility of Li^+ and conductance measurements in a borosilicate microchannel. We quantified zeta potential, ζ, as a function of concentration for Alexa Fluor 488 and sodium Fluorescein concentrations in a set of preliminary calibration experiments. We used the current monitoring technique[23] in a 10 μm high, 70 μm wide borosilicate microchannel (Caliper Life Sciences, Mountain View, CA). Separate current monitoring experiments using 1 mM Alexa Fluor in a 1 μm high fused silica microchannel (negligible EDL) fabricated with the same technique and materials used for microchannel–nanochannel devices gave results within 8% of the measured ζ in borosilicate.

From the ζ measurements shown in Figure 3, we estimate wall ζ as a function of dye concentration according to a power law fit:

$$\zeta = -ac_r^b \qquad (7)$$

A least-squares fit provides excellent agreement to the data with $a = 0.0553$ V/mM^b and $b = -0.261$ for Alexa Fluor 488 as the electrolyte and $a = 0.0760$ V/mM^b and $b = -0.122$ for Fluorescein. Calculations of shear plane charge (hereafter "wall charge") from Guoy–Chapman theory[24] on the basis of measured ζ potentials showed a $\sim c_r^{-0.33}$ dependence for Alexa Fluor 488. To find a scaling for ζ inside the nanochannel, ζ_n, we used this calculated wall charge and the theoretical result that $c_n \sim 0$ for most experimental cases and found that $\zeta_n \sim c_r^0$. These data are used later to analyze trends in measured shock velocities and enrichment region concentrations.

Device Fabrication. We fabricated microchannel–nanochannel devices using conventional photolithography, dry etching, and bonding techniques.[25,26] Nanochannel sections were 49 and 97 nm high (corresponding to nominal heights of 50 and 100 nm), and all microchannel sections were 1 μm high. All sections were 20 μm wide (in plane). The region over which height changes between the nanochannel and the microchannels is $\sim$2 μm long (determined by physics of our photolithography and etching). We characterized channel height using a Dektak profilometer (Veeco Instruments, Santa Barbara, CA).

CP and Imaging Protocol. We filled our channels with dye solution via pressure-driven flow (40 min at $\sim$1 atm) before each experiment. For more information on channel conditioning, see the Supporting Information. Upon application of 1 nA currents, voltage (which was automatically regulated by the high-voltage source-and-measure power supply) typically increased from zero to about 200 V over 2 min and then increased steadily over the remainder of the experiment ($\sim$10 min). We recorded images at 0.5–10 fps depending on the applied current density. We corrected all images using flatfield and background images acquired before and after each experiment, respectively. We smoothed images with negligible loss in resolution using a Gaussian filter with a standard deviation of 1.5 μm.

Results and Discussion

Scaling Derivation from Simple Model. We here present some key scaling arguments of Part I which serve to frame the numerical results, yield intuition, and help explain observed

experimental trends. In Part I, we predicted that the enrichment shock velocity is equal to the bulk velocity in the microchannel. Therefore, assuming the nanochannel is the dominant pressure resistance (a good assumption for our geometry), the enrichment shock velocity is

$$V_5 = \frac{Q}{h_m} \approx \frac{U_n^{EOF} h_n}{h_m} \qquad (8)$$

where Q is the bulk flow rate, U_n^{EOF} is the area-averaged electroosmotic flow (EOF) velocity in the nanochannel, and h_m and h_n are the microchannel and nanochannel heights, respectively. Therefore, in terms of the experimental parameters

$$V_5 \approx \left(\frac{\varepsilon}{h_m \eta}\right) \frac{\zeta_n h_n I}{G_n} \qquad (9)$$

where G_n is the nanochannel conductance, ε is permittivity, ζ_n is nanochannel zeta potential, η is viscosity, and I is the applied current. For small $c_n^* h_n^* = (\nu_1 z_1 - \nu_2 z_2) F h_n c_n / (-2\nu_1 \sigma)$, nanochannel conductance is approximately independent of the channel height and is proportional to σ,[27] and $V_5 \sim \zeta_n h_n I / \sigma$. Initial nanochannel wall charge is taken as a function of c_r. We use these scalings to examine trends in our measurements of enrichment shock velocity.

Similarly, we can derive an equation relating the depletion shock velocity to the applied current. On the basis of eqs 41–44 of Part I and the scaling for bulk velocity given by eq 8

$$V_1 = V_5 - \left(\frac{\varepsilon}{h_m \eta}\right) \frac{\zeta_n h_n}{G_n} \frac{I}{c_r^* h_n^*} \frac{c_5^* h_n^*}{c_r^* h_n^*} \qquad (10)$$

where from eqs 43 and 45, $c_5^* h_n^* = \nu_{2n}^*$ for $\nu_{2n}^* < 1$ and $c_5^* h_n^* = (2\nu_{2n}^* - 1)$ for $\nu_{2n}^* \geq 1$. Assuming $G_n \sim \sigma$, $(V_1 - V_5) \sim \zeta_n h_n I / \sigma \cdot c_5^* h_n^* / c_r^* h_n^*$. Physically, there are two contributions to V_1: One is due to bulk flow, which is equal to V_5, and one is driven by current through the EDLs. Therefore, the quantity $(V_1 - V_5)$ is the portion of the depletion region shock velocity which is driven by current through the EDLs. We will show that measured $(V_1 - V_5)$ is proportional to applied current and scales as predicted by eq 10.

Next, we derive a scaling for the measured cathode side enrichment ratio, c_5/c_r, which sets the electric field in the cathode side microchannel. On the basis of eqs 41 and 43 of Part I,

$$\frac{c_5}{c_r} = \frac{c_5^* h_n^*}{c_r^* h_n^*} \qquad (11)$$

where, again, $c_5^* h_n^* = \nu_{2n}^*$ for $\nu_{2n}^* < 1$ and $c_5^* h_n^* = (2\nu_{2n}^* - 1)$ for $\nu_{2n}^* \geq 1$. Hence, the enrichment region concentration ratio is independent of applied current. Later, we will show experimental evidence which demonstrates this somewhat nonintuitive result.

Finally, using the analytical results of Part I, we can derive a simple relation among all of the experimentally measurable parameters, c_5, c_r, V_1, and V_5. Substituting Part I, eq 41 into eq 42, or Part I eq 43 into eq 44, yields

$$\frac{c_5}{c_r} = 1 - \frac{V_1}{V_5} \qquad (12)$$

This expression is a general result which can be derived from a much simpler control volume analysis and the observation that $c_1 \sim 0$. Conserving species, current, and bulk velocities in the large control volume, CV$_{total}$, of Figure 1a, we see the net

(23) Sze, A.; Erickson, D.; Ren, L.; Li, D. *J. Colloid Interface Sci.* **2003**, *261*, 402–410.

(24) Hunter, R. J. *Zeta Potential in Colloid Science*; Academic Press: London, 1981.

(25) Jacobson, S. C.; Moore, A. W.; Ramsey, J. M. *Anal. Chem.* **1995**, *67*, 2059–2063.

(26) Pennathur, S.; Santiago, J. G. *Anal. Chem.* **2005**, *77*, 6782–6789.

(27) Schoch, R. B.; van Lintel, H.; Renaud, P. *Phys. Fluids* **2005**, *17*, 100604.

accumulation, Σ_{total}, is zero. Dividing this region into two respective CVs for the anode and cathode sides, we write $\Sigma_{anode} + \Sigma_{cathode} = 0$, so the rate of concentration depletion on the anode side is proportional to $(c_r - c_1)V_1 \approx c_r V_1$. This is equal to the rate at which the concentration increases on the cathode side

$$c_r V_1 = (c_r - c_5)V_5 \qquad (13)$$

Equations 12 and 13 are equivalent derivable from a CV analysis which yields intuition about system-wide reorganization of charge. CP redistributes ionic strength from the anode side of the nanochannel (forming depletion) to the cathode side (creating enrichment).

Numerical Results. Figure 1b and 1c shows two illustrative anecdotal results of the computations. Figure 1b shows a representative computation for a propagating CP case with $c_r^* h_n^* = 0.71$ and $\nu_{2n}^* = 0.7$. Under these conditions, CP formed an anode-side depletion region with $c_1 \approx 0$ and a cathode side enrichment region with $c_5 > c_r$. At these values of $c_r^* h_n^*$ and ν_{2n}^*, we see the CP depletion and enrichment regions at the anode- and cathode-side nanochannel interfaces. However, unlike classic, stationary models, the computational model captures transient propagation of CP depletion and enrichment regions which propagate toward the anode and cathode, respectively.

Figure 1c shows a representative computation for $c_r^* h_n^* = 0.85$ and $\nu_{2n}^* = 0.37$. In this regime of the $c_r^* h_n^*$ and ν_{2n}^* map, the depletion region characteristic velocity is positive, and so CP enrichment and depletion shocks do not propagate (cf. Figure 5). Here, the steady-state concentrations in both the anode- and cathode-side microchannels are approximately equal to the initial concentration. The region just downstream of the nanochannel shows a slight enrichment versus that just upstream (as discussed in Part I). As predicted by the analytical results presented in Part I, the nanochannel concentration quickly decreases (to 55% of its initial value) within a few hundred milliseconds. As the nanochannel concentration adjusts to its steady-state value, the cathode side interface collects ionic strength and causes a slight increase in c_0 which moves at the bulk velocity through the cathode-side microchannel. (In the CP propagation case of Figure 1b, the adjustment of the concentration in the nanochannel also causes a slight local maxima in concentration near the leading edge of the enrichment shock.)

Figure 4a, 4b, and 4c shows predicted spatiotemporal plots of the ion concentration in the series micro-nano−microchannel system as a function of the axial coordinate and time. The model parameters are identical to those of the experiments (discussed below). White/yellow color indicates high concentration (enrichment), and black represents low concentration (depletion). Figure 4a shows predictions for a constant current of 200 pA and a 50 nm high nanochannel. We used the known mobility of Li$^+$ ion and the measured mobility of the Alexa Fluor 488 dianion (as determined from independent experiments). We assumed the microchannel wall charge was constant and uniform, and we determined this using the measured zeta potential at the initial concentration of 1 mM. We found excellent agreement with experimental results for $\sigma_{nano} = 0.25\sigma_{micro}$ (and this empirical value of 0.25 constitutes our only fitting parameter). The enrichment and depletion shocks spread as straight lines on this plot indicating a constant shock velocity. Figure 4b shows computations for the same conditions and geometry as in Figure 4a but with a constant current of 800 pA. As predicted by the analytical model of Part I and the current numerical model, the enrichment and depletion shock velocities are directly proportional to current density. Also, there is a diffuse leading edge of the enrichment region for the 800 pA case and an increased width of this transition in the 200 pA case.

Figure 4c shows a spatiotemporal plot for a sample case where CP enrichment and depletion shocks do not propagate (and CP is slight and confined to near-interface regions). This case corresponds to 10 mM sodium Fluorescein and a 100 nm high nanochannel. Here, we did not use a fitting parameter; we fixed both the microchannel and nanochannel wall charge on the basis of independently measured ζ. As shown in Figure 1c, a small "bump" region of increased concentration advects away from the nanochannel into the cathode-side microchannel (note the slight contour ridge at about 30° from the vertical on the cathode side). Other than this slight transient, the rest of the microchannel sections remained at the initial concentration. The nanochannel adjusted to a new concentration 12% lower than the initial value.

Figure 5 shows contours of c_5/c_r at steady state computed with our area-averaged (one-dimensional) computational model. (The simple model of Part I well predicts trends in c_5/c_r, but the computational model better accounts for the effects of EDL.) Here, c_5 is measured ~10 μm away from the cathode-side interface. These results show that c_5/c_r decreases smoothly as $c_r^* h_n^*$ increases and ν_{2n}^* decreases. We also show a contour of $U_1/V_5 = 0$, where U_1 is the characteristic velocity in the depletion region ~10 μm away from the anode-side interface. This provides a practical definition of the boundary between the regions where CP shocks propagate and where they do not ("no propagation"). The strong depletion shocks characteristic of CP with propagation can only occur when U_1 is negative. Figure 5 also shows the predicted phase boundary on the basis of the simple model of Part I as a gray dashed line.

Experimental Results. We performed a fairly extensive experimental parametric variation of key parameters. This includes over 100 realizations at 30 conditions. Experiments were performed at nanochannel heights of 50 and 100 nm, and seven applied currents ranging from 50 pA to 16 nA. We used nine electrolyte solutions ranging from 100 μM to 10 mM sodium Fluorecein and 50 μM to 1 mM Alexa Fluor 488. Here, we present a summary of these experiments and comparisons with our numerical predictions. We also compare trends to those predicted by the analytical model of Part I.

Figure 4d and 4e shows measured spatiotemporal plots for a channel initially filled with a uniform concentration of Alexa Fluor 488 dye and constant applied currents at the conditions of Figure 4a and 4b, respectively. First, we see that the enrichment and depletion concentration shock motions and widths were consistent with the high PeL/h regime predicted and discussed in Part I (the PeL/h values for these cases are 54.4 and 165, respectively). The flow was clearly in a regime where propagations of enrichment and depletion zones are clearly observable and shock widths are much shorter than channel lengths. The enrichment and depletion shocks were linear confirming the computational prediction that the shock velocities are constant in time. The shock velocities are also proportional to current density as predicted by eqs 9 and 10 (confirmed in Figure 6). The shock widths of the 800 pA case are also smaller than those of the 200 pA case as predicted. (There is significant enrichment/depletion and CP propagates, yet the EDLs do not overlap for these cases with $\lambda_D = 6.4$ nm and $h = 50$ nm.)

Figure 4f shows sample experimental results for a reservoir concentration of 10 mM Fluorescein (same as Figure 4c). For these conditions, the flow field is also in the high PeL/h limit (here, $PeL/h = 49$) but in the regime where CP occurs but does not propagate as predicted (e.g., see Figure 1c). A small disturbance in concentration advected away from the nanochannel at constant positive velocity. This disturbance is predicted by the computational model and, as discussed above, is caused by the
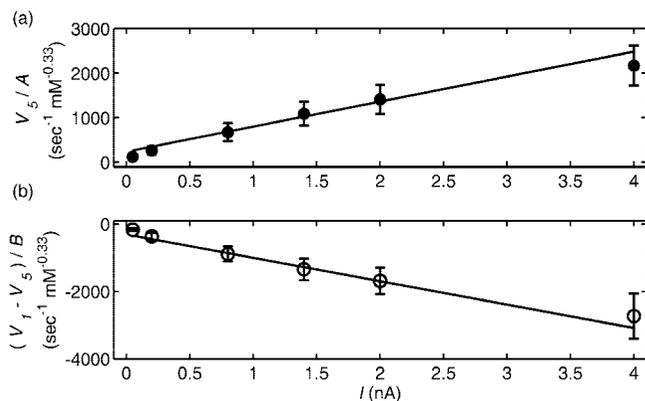
Figure 6. Measurements of enrichment (a) and depletion (b) shock velocities versus applied current for Alexa Fluor 488 experiments. In a, we plot the enrichment shock velocity, scaled by A, where $A = h_n c_r^{0.33}$, and b presents the depletion shock minus enrichment shock velocity, scaled by B, where $B = h_n c_r^{0.33}(c_5^* h_n^*/c_r^* h_n^*)$. Data represent experiments with $h_n = 50$ nm and 50 μM, 100 μM, and 1 mM dye concentrations as well as $h_n = 100$ nm and 100 μM dye concentration. We assumed σ varies with concentration according to a power law on the basis of ζ potential measurements (this accounts for the fractional power in the scaling). ν_{2n}^* and $c_r^* h_n^*$ were computed as in Figure 5. A solid black line shows a linear regression fit to all of the data. Error bars show 95% confidence intervals on the mean with $N \geq 12$. Shock velocities were computed by performing a linear least-squares fit to the edge of the enrichment or depletion region on 73 spatiotemporal plots of concentration versus time (as shown in Figure 4). Shock velocities are clearly linearly proportional to current density as predicted by the model.

readjustment of the nanochannel concentration to its steady-state value. The typical disturbance observed in experiments was sharper (narrower in space) than that predicted by the model as shown here. The experiment of Figure 4f also showed ~20 μm wide stationary, nonpropagating regions of depletion and enrichment adjacent to the interfaces from the nanochannel. A diffusive depletion region is observed in the computations, although the predicted width of this region is ~100 μm; the local enrichment is barely apparent in computations.

Direct comparison of our experimental results to previous experimental visualizations of CP is very difficult and could be misleading. One difficulty is that previous work has studied more complex geometries, such as intersections between multiple nanochannels and microchannels[1,2,9,10] or the CP type effects around randomly packed spheres,[28,29] membranes,[13] or ion-permselective polymers.[4,11] Most importantly, comparison is made very difficult because we know of no other work which uses a fluorescent ion as one of two background electrolyte ions present in highest concentration as we do here. Instead, all previous work in visualizaing CP[1,2,4,9,10,13,28,29] used an ionic, fluorescent species in low concentration relative to the background electrolyte. Such species may focus either because of CP or because of effects such as electrophoretic focusing of a single species in the background electric field gradients set up by CP of background electrolytes. In the latter case, fluorescent species accumulate and concentrate in regions where electrophoretic velocity is balanced by bulk velocity. We have published a preliminary analysis of the latter effect[3] and will address this in more detail in future work.

We performed experiments at conditions spanning 10 combinations of $c_r^* h_n^*$ and ν_{2n}^*. A comparison between the predicted propagation versus no propagation regime map and the experimental observations is shown in Figure 5. Experiments where

CP shocks clearly propagated are shown as filled circles, while experiments where CP did not propagate are shown as open triangles. The $c_r^* h_{2n}^*$ and ν_{2n}^* regime alone is an excellent predictor of whether CP shocks will propagate. All of the experimentally observed CP propagation cases fall within the predicted CP with propagation region. Similarly, "no propagation" cases fall in the correct region. The open triangle nearest the $U_1/V_5 = 0$ boundary (at $\nu_{2n}^* = 0.45$ and $c_r^* h_n^* = 1.3$) showed a hybrid behavior. For this case alone, the results show an initial (weak) development of CP with propagation followed by a decrease in cathode-side concentration and a reversal of shock velocities.

In Figure 5, we label the enrichment concentration ratio c_5/c_r for the experimental data where ion enrichment intensity was sufficiently above the noise for us to measure (these values can be compared to the c_5/c_r contours of the plot). The comparison shows that the theory is only a fair-to-good predictor of the absolute value of the enrichment ratio; differences between the predicted and observed absolute values of c_5/c_r from Alexa Fluor 488 experiments range from $\pm 20\%$. We hypothesize the discrepancy is related to the difficulties associated with accurate predictions of the nanochannel wall charge. As seen in Figure 4, we can well predict c_5/c_r if we use nanochannel wall charge as a fitting parameter.

Next, we present trends in measured depletion and enrichment shock velocities. To quantify shock velocities from measured spatiotemporal plots of fluorescence intensity (see Figure 4d and 4e), we thresholded the data (at approximately 10% and 50% of max intensity) to create binary images. We then used a simple edge-detection algorithm to identify 100−200 points along the shock boundaries, and we used a linear regression to measure velocity. For many cases, enrichment and depletion shocks showed noticeable curvature over the first ~10 s. This behavior was also observed in computations and appears to be associated with initial transients in the nanochannel. In these cases, the reported shock velocity is measured after this initial transient. Other nonconstant shock velocity behaviors are discussed in the Supporting Information document.

Figure 6 shows scaled enrichment and depletion shock velocity measurements versus applied current. The shock velocities are scaled according to eqs 9 and 10 using the empirical relation for wall charge on the basis of independent ζ measurements as well as ν_{2n}^* and $c_r^* h_n^*$ computed as in Figure 5. The shock velocities, which varied from 0.7 to 282 μm/s, varied proportionally with current density and were collapsed by the scaling. These magnitudes (and the strong concentration changes they propagate) are striking evidence to the importance of these shocks in determining the behavior and performance of hybrid micro- and nanochannel systems.

Figure 7 shows the measured c_5/c_r divided by the predicted concentration factor, $c_5^* h_n^*/c_r^* h_n^*$, versus applied current.[30] The scaled enrichment region concentration factor showed approximately no dependence on current density, as predicted by theory, confirming that (perhaps counterintuitively) the magnitude of CP enrichment is not affected by current density. The mean value of the measured enrichment concentration factor divided by the predicted value is 1.3 demonstrating that the simple theory of Part I can be used as a fair predictor of c_5/c_r without fitting parameters or transient simulations. Raw data for c_5/c_r (insert) shows the significant scatter in the unscaled data (on average,

(28) Ehlert, S.; Hlushkou, D.; Tallarek, U. *Microfluid. Nanofluid.* **2007**, *4*, 471–487.

(29) Leinweber, F. C.; Tallarek, U. *Langmuir* **2004**, *20*, 11637–11648.
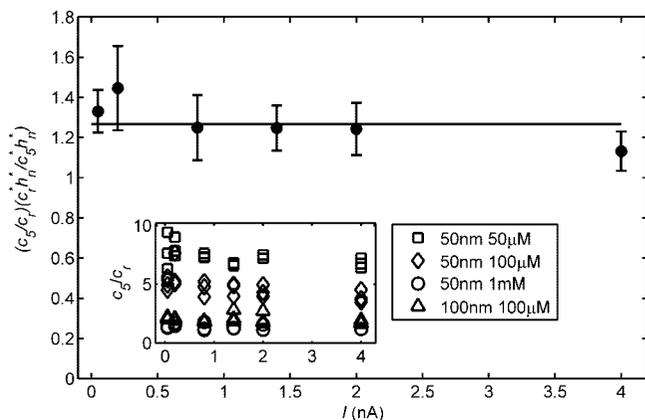
Figure 7. Scaled enrichment region concentration, $c_5/c_r(c_r^*h_n^*)/(c_5^*h_n^*)$, versus applied current. The line shows the average of all data as a visual reference. We computed v_{2n}^* and $c_r^*h_n^*$ for prediction of $c_5^*h_n^*/c_r^*h_n^*$ according to Part I eqs 41 and 43 using the same parameter values as in Figure 5. Error bars show a 95% confidence interval on the mean at each value with $N \geq 12$. The insert shows raw, unscaled data for enrichment-to-initial ion density. As predicted, the scaled concentration data are approximately constant versus current.
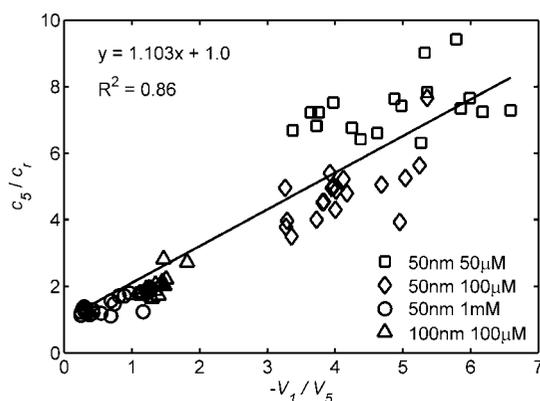
Figure 8. Background electrolyte enrichment factor, c_5/c_r, versus depletion-to-enrichment shock velocity ratio for 73 realizations. The solid line is a least-squares best fit line with a fixed y-intercept of 1.0. The model predicts a linear dependence, and we see it collapses the data very well for values of $-V_1/V_5$ below about 2 and adequately for larger values. This greater scatter may be due to the influence of impurity ions (e.g., carbonate) which were not controlled for in experiments.

c_5/c_r varies by a factor of ~ 7, while our scaled parameter varies by ~ 1.7).

Last, we present a collapse of all of the measured concentration and shock velocity data for the 73 relevant (CP with propagation) Alexa Fluor 488 experiments. Figure 8 shows the enrichment factor, c_5/c_r, versus the depletion-to-enrichment shock velocity

---

(30) To quantify the enrichment region concentration, we averaged fluorescence intensities in a 200 pixel box after any initial, transient concentration increases. We assume the flatfield-corrected dye intensity is proportional to concentration. Quantitative measures of the depletion region concentration were not possible as most measured intensities were within the noise level. This result is consistent with the analytical prediction that the depletion region concentration is much less than the initial concentration.

---

ratio. All experiments approximately collapsed to one line as predicted by eq 12. Figure 5 shows a regression fit with y-intercept fixed to 1.0, consistent with experimental observations for cases where CP shocks did not propagate. In these experiments, V_1 was 0.0 μm/s, and c_5/c_r was 1.0 (see Figure 4f). The fit line has a slope of 1.1 in good agreement with the predicted value of 1.0.

Conclusions

We have developed a computational model which accurately predicts the existence of CP with propagating enrichment and depletion shocks in a microchannel−nanochannel system on the basis of separately determined zeta potential and ion mobilities. We presented the first experimental observations of CP in which the concentration field of the background electrolyte is directly observed and quantified. Experiments performed at constant current conditions showed constant growth of enrichment and depletion regions with time validating our computational model and clearly demonstrating the predicted behavior of CP with propagation. The measured enrichment and depletion shock velocities scaled as predicted by Part I. In particular, the shock velocities increased linearly with current density suggesting that, in a microchannel system, the extent of CP is determined by the current through the nanochannel. The magnitude of the CP enrichment relative to the reservoir concentration, c_5/c_r, also scaled as predicted by Part I and was essentially independent of current density.

For individual experimental conditions, we found excellent agreement to computational results using nanochannel wall charge as a single fitting parameter. This agreement includes the generation of depletion and enrichment zones on the anode and cathode sides of the nanochannel, the propagation of these zones upstream and downstream of the nanochannel, and trends in the ion concentration shock widths with current density. Overall, the results suggest that CP and its propagation can have long-range effects on the concentration in hybrid microchannel−nanochannel systems. These effects must be considered in the design of hybrid devices which attempt to leverage nanochannel physics.

Supporting Information Available: Discussion of channel-conditioning procedure, additional spatiotemporal plots showing the effects of increasing current density, and discussion of spatiotemporal plots showing nonlinear growth of enrichment and depletion regions. This information is available free of charge via the Internet at http://pubs.acs.org.

LA803318E